AGU PUBLICATIONS

JGR

Journal of Geophysical Research: Solid Earth

RESEARCH ARTICLE

10.1002/2014JB011223

This article is a companion to *Salmi et al.* [2014] doi:10.1002/2014JB011086.

Key Points:

- Reduced magnetization at both active and inactive hydrothermal deposits
- Raven site is approximately 15 million cubic meters in volume
- Magnetization represents static time-averaged hydrothermal alteration

Supporting Information:

- Figure S1
- Figure S2
- Figure S3
- Text S1

Correspondence to:
M. A. Tivey,
mtivey@whoi.edu

Citation:
Tivey, M. A., H. P. Johnson, M. S. Salmi, and M. Hutnak (2014), High-resolution near-bottom vector magnetic anomalies over Raven Hydrothermal Field, Endeavour Segment, Juan de Fuca Ridge, *J. Geophys. Res. Solid Earth*, *119*, 7389–7403, doi:10.1002/2014JB011223.

Received 24 APR 2014
Accepted 17 JUL 2014
Accepted article online 1 SEP 2014
Published online 6 OCT 2014

High-resolution near-bottom vector magnetic anomalies over Raven Hydrothermal Field, Endeavour Segment, Juan de Fuca Ridge

Maurice A. Tivey[1], H. Paul Johnson[2], Marie S. Salmi[2], and Michael Hutnak[3]

[1]Department of Geology and Geophysics, Woods Hole Oceanographic Institution, Woods Hole, Massachusetts, USA, [2]School of Oceanography, University of Washington, Seattle, Washington, USA, [3]Earth and Planetary Science, University of California, Santa Cruz, California, USA

Abstract High-resolution, near-bottom vector magnetic data were collected by remotely operated vehicle *Jason* over the Raven hydrothermal vent field (47°57.3′N 129°5.75′W) located north of Main Endeavour vent field on the Endeavour segment of the Juan de Fuca Ridge. The survey was part of a comprehensive heat flow study of the Raven site using innovative thermal blanket technology to map the heat flux and crustal fluid pathways around a solitary hydrothermal vent field. Raven hydrothermal activity is presently located along the western axial valley wall, while additional inactive hydrothermal deposits are found to the NW on the upper rift valley wall. Magnetic inversion results show discrete areas of reduced magnetization associated with both active and inactive hydrothermal vent deposits that also show high conductive heat flow. Higher spatial variability in the heat flow patterns compared to the magnetization is consistent with the heat flow reflecting the currently active but ephemeral thermal environment of fluid flow, while crustal magnetization is representative of the static time-averaged effect of hydrothermal alteration. A general NW to SE trend in reduced magnetization across the Raven area correlates closely with the distribution of hydrothermal deposits and heat flux patterns and suggests that the fluid circulation system at depth is likely controlled by local crustal structure and magma chamber geometry. Magnetic gradient tensor components computed from vector magnetic data improve the resolution of the magnetic anomaly source and indicate that the hydrothermally altered zone directly beneath the Raven site is approximately 15×10^6 m^3 in volume.

1. Introduction

Hydrothermal circulation within oceanic igneous basement is a fundamental process at mid-ocean ridge spreading centers responsible for the physical and chemical evolution of the crustal rocks, the deposition of metal-rich, economically valuable minerals, and for the colonization by unique biological communities [e.g., *Alt*, 1995; *Stein and Stein*, 1994; *Mottl*, 2003; *Hannington et al.*, 2005; *Childress and Fisher*, 1995]. The magnitude, pathways, and extent of subsurface fluid circulation are difficult to constrain at an active mid-ocean ridge, especially where sediment cover is minimal and direct conductive heat flux measurements are not possible with conventional heat flow probes. Moreover, it has also been difficult to determine the conductive heat flux in and around vent sites at the resolution required for the sub-100 m scale of hydrothermal vent fields. Insight into the geometry of subsurface hydrothermal circulation related to vent sites has been previously provided from an unlikely source. High-resolution magnetic field mapping has revealed discrete zones of demagnetized crust associated with hydrothermal vent deposits in basaltic-hosted seafloor inferred to represent patterns of subsurface upflow [e.g., *Tivey et al.*, 1993, 1996; *Tivey and Johnson*, 2002; *Tivey et al.*, 2003; *Tivey and Dyment*, 2010; *Zhu et al.*, 2010; *Honsho et al.*, 2013]. It is well established that the destruction of iron-titanium oxide minerals carrying magnetic remanence in oceanic basalt is a direct result of hydrothermal alteration [*Ade-Hall et al.*, 1971; *Watkins and Paster*, 1971; *Rona*, 1978; *Wooldridge et al.*, 1990], in contrast to the more systematic and ubiquitous low temperature alteration experienced by oceanic crust as it ages [e.g., *Irving*, 1970; *Johnson and Merrill*, 1972, 1973; *Johnson and Atwater*, 1977]. Ancient analogs of hydrothermal systems in ophiolites show that discrete zones of demagnetized crust are associated with the heavily mineralized stockworks of ore deposits producing discrete magnetic anomalies [e.g., *Richards et al.*, 1989; *Johnson et al.*, 1982; *Hall*, 1992]. Furthermore, studies of hydrothermal systems on land in volcanic settings show that alteration is by far the most dominant mechanism for the destruction of magnetic minerals [e.g., *Studt*, 1959; *Browne*, 1978; *Hochstein and Soengkono*, 1997] compared to the transient thermal demagnetization of magnetic minerals due to temperatures elevated above the Curie temperature.

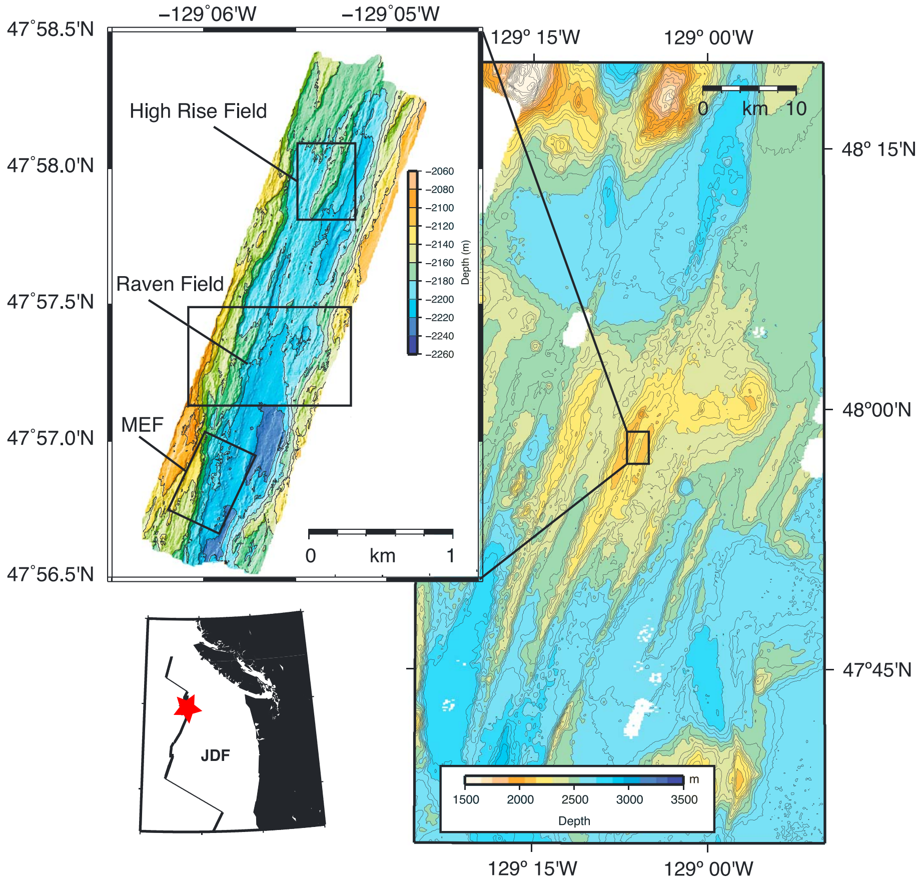

Figure 1. Location bathymetry map of Endeavour Ridge rift valley on the Juan De Fuca Ridge in the NE Pacific showing the location of the Raven hydrothermal field relative to the Main Endeavour vent Field (MEF) and the High Rise vent field. Inset map shows location of Raven survey (red star) on northern Juan de Fuca Ridge.

High-resolution seafloor magnetic mapping at the Main Endeavour Field (MEF) on the Juan de Fuca Ridge provided the first tangible evidence of tightly constrained subsurface fluid upflow zones that are potentially associated with hydrothermal vent systems [*Tivey and Johnson*, 2002]. Patterns of demagnetization suggested that discrete and sharply defined zones of upflow were associated with the primary hydrothermal vent structures within the MEF vent field and that both active and inactive vent sites were associated with well-defined magnetic "burnholes," i.e., discrete zones of reduced crustal magnetization [*Tivey and Johnson*, 2002]. There are now abundant examples of similar magnetic "burnholes" present in a variety of basaltic-hosted hydrothermal settings such as mid-ocean ridges, seamounts, and back-arc environments [e.g., *Tivey and Dyment*, 2010; *Zhu et al.*, 2010; *Caratori-Tontini et al.*, 2012; *Honsho et al.*, 2013].

Models of mid-ocean ridge hydrothermal fluid circulation have evolved from large-scale spreading center-scale circulation [*Phipps Morgan and Chen*, 1993; *Chen and Morgan*, 1996; *Wilcock*, 1998] to more localized circulation models that utilize high-permeability pathways provided by faults and topography [e.g., *Rabinowicz et al.*, 1999; *Spinelli and Fisher*, 2004; *Lowell et al.*, 2012, 2013]. Recent numerical models of hydrothermal fluid circulation show that circulation can be highly localized around vent systems with annular zones of recharge in close proximity to the upflow zones [e.g., *Fontaine and Wilcock*, 2007; *Coumou et al.*, 2008].

In the following study, we investigate the detailed magnetization of a small region associated with an isolated vent site, the Raven vent field on the northern Juan de Fuca Ridge. The magnetic survey was an integral part of a study of an active vent site using a novel technology designed to allow for detailed heat flux measurements where conventional heat flow probe measurements are not possible [*Johnson and Hutnak*, 1997; *Johnson et al.*, 2010; *Salmi et al.*, 2014]. The combination of these two detailed data sets along with seafloor geological observations [*Hearn et al.*, 2013] allow us to compare, for the first time,

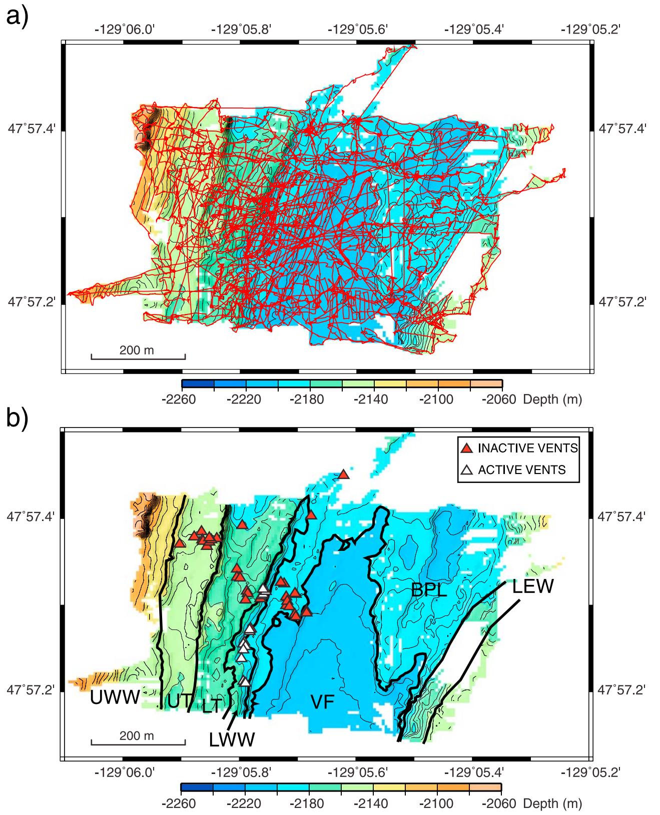

Figure 2. (a) High resolution ROV *Jason* multibeam bathymetry map (SM2000 [*Johnson et al*., 2002]) of the Raven hydrothermal field area showing the *Jason* track lines (red) which collected magnetic field and bathymetry data. Contour interval is 5 m. (b) Bathymetry map of the Raven vent field study area showing the location of the active (white triangles) and inactive (red triangles) hydrothermal vent sites and the major tectonic zones from west to east: upper west wall (UWW), upper terrace (UT), lower terrace (LT), lower west wall (LWW), valley floor (VF), broken pillow lavas (BPL), lower east wall (LEW). Contour interval is 5 m.

the geometry inferred from magnetic subsurface crustal structure with measured conductive heat flux patterns and seafloor permeability data.

2. The Raven Field-Endeavour Ridge

The 90 km long Endeavour Ridge (Figure 1) is a mid-ocean ridge segment of the intermediate rate spreading Juan de Fuca Ridge system that features an elongate volcanic ridge with a central graben axial valley, which hosts several major high-temperature hydrothermal vent fields systematically spaced several kilometers apart [*Delaney et al*., 1992, 1997; *Glickson et al*., 2007; *Kelley et al*., 2012]. These vent fields, from south to north, include Mothra, Main Endeavour vent Field (MEF), High Rise vent Field, Salty Dawg, and Sasquatch [*Kelley et al*., 2012]. Multichannel seismic imaging shows that an Axial Melt Chamber (AMC) is present beneath the central 25 km section of the ridge segment at a depth of 2.2 to 2.5 km [*Van Ark et al*., 2007; *Carbotte et al*., 2012]. The AMC appears to be subdivided along strike into three main bodies with boundaries at 47°54.7′N, 47°56.8′N and 48°00.5′N, which is also reflected in the overall morphology of the ridge segment topography [*Carbotte et al*., 2012; *Kelley et al*., 2012]. Seismic imaging of the upper crustal extrusive lava section (i.e., Layer 2A) suggest that its thickness ranges from 330 m beneath the rift valley to 550 m on the flanks of the ridge [*Van Ark et al*., 2007]. The depth of the rift valley graben correlates with the depth of the AMC, with the deepest portion of the graben overlying the shallowest AMC. This suggests that rather than being generated by amagmatic extension, the axial graben is formed as a response to magma withdrawal from a steady state magma lens, subsequent dike injection, and the resultant faulting [*Carbotte et al*., 2006]. Supporting this model are microseismic earthquake studies that show that the bounding axial rift valley faults extend down to the edges of the AMC between MEF and High Rise fields [*Wilcock et al*., 2009].

Hydrothermal activity was initially thought to be limited to the five major vent fields, spaced 2–3 km apart [*Delaney et al*., 1992; *Wilcock and Delaney*, 1996], but it is now recognized that hydrothermal activity is more widely distributed with smaller and less active areas located between these major fluid emission sites [*Johnson et al*., 2002; *Glickson et al*., 2007; *Clague et al*., 2008; *Jamieson et al*., 2013; *Kelley et al*., 2012]. The Raven hydrothermal vent field (Figure 1) is an example of one of these small vent sites located ~400 m north of MEF and ~1800 m south of High Rise Field. The Raven Field (Figure 2a) was discovered in 2001 during a remotely operated vehicle (ROV) survey of the near bottom geology and diffuse vent flux output [*Johnson et al*., 2002]. The Raven Field is comprised of a central ~10 m tall, largely inactive chimney complex directly adjacent to the western rift valley wall, with standing and toppled sulfide chimneys extending over to the western wall where active venting >200°C was located in 2001. Hydrothermal activity was found to extend more than 100 m south along this western wall [*Johnson et al*., 2002]. In 2011, the area of >200°C

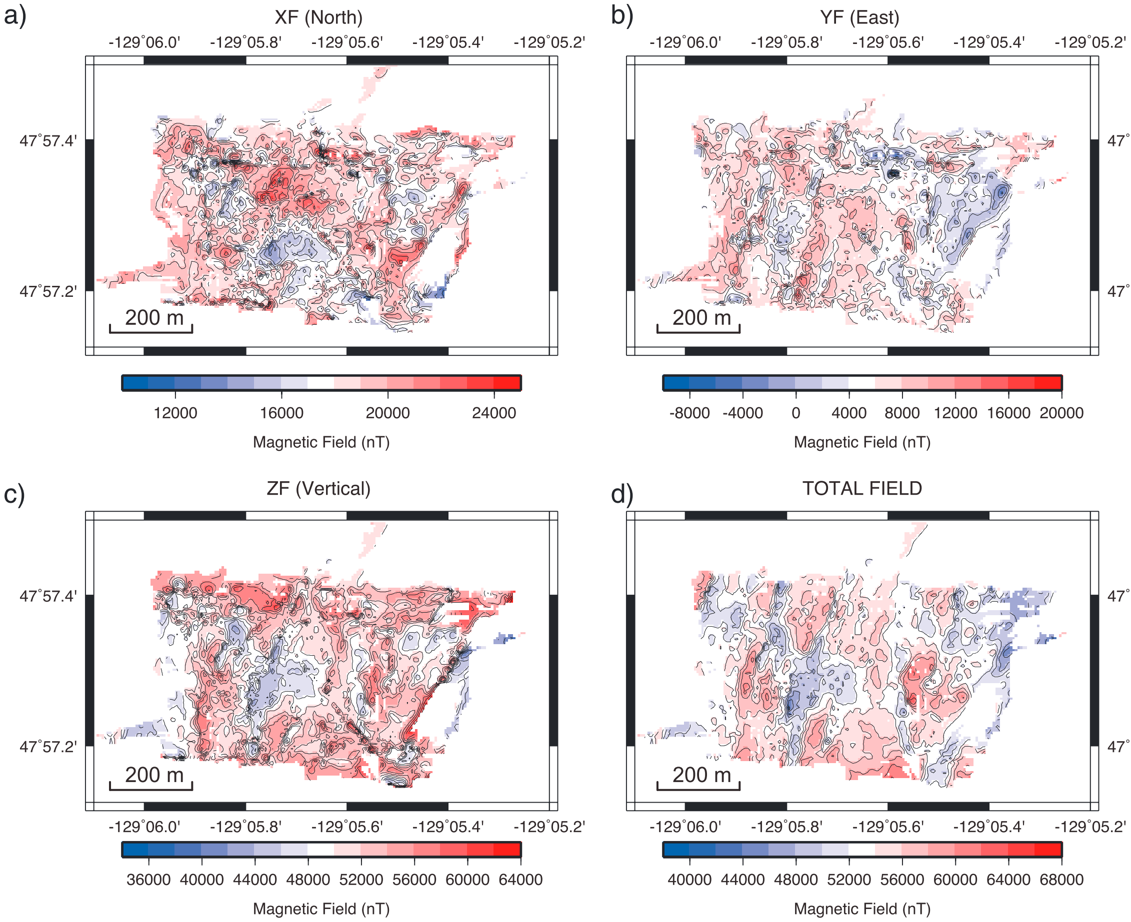

Figure 3. Panel of four maps showing the three observed magnetic field components measured along the uneven ROV survey (i.e., varying depth and height above seafloor): (a) North, (b) East, and (c) Vertical components, corrected for the motion of ROV *Jason* and the vector summed (d) Total magnetic field. Contour interval is 2000 nT except for the north component which is 1000 nT.

venting had died down to low-level diffuse activity, while active high-temperature venting had shifted ~100 m south along the rift valley wall [*Hearn et al*., 2013].

The relatively isolated nature of the Raven vent field presented an opportunity to examine a vent field system that could be constrained by a single-field program and potentially address universal questions regarding the geometry and extent of fluid recharge and discharge of hydrothermal systems. We report here on the magnetic survey completed over this site as part of a larger heat flux survey [*Salmi et al*., 2014] and then discuss the implications and relationship between the interrelated data sets.

3. Methods

In 2011, an R/V *Atlantis* research cruise (AT18-09) conducted a remotely operated vehicle (ROV) *Jason II* survey of the Raven vent field area (Figure 2a). One of the primary objectives of the field program was to perform a conductive heat flux survey of the rift valley and region immediately surrounding the Raven vent site [*Hearn et al*., 2013; *Salmi et al*., 2014]. Another key objective was to undertake a detailed magnetic field survey of the study area. A three-axis Honeywell HMR2300 magnetometer was mounted to ROV *Jason*, and during transits, between heat flow stations, ROV *Jason* photographically imaged the seafloor geology and collected underway magnetic field data of the axial valley seafloor and walls (Figure 2b). Three ROV *Jason* dives (586, 590, and 591) collected multiple overlapping track lines within an area of ~700 by 450 m (Figure 2a). For each ROV dive, a calibration spin of the vehicle on descent and on ascent was performed to compute the calibration coefficients required to correct the magnetic data for the effects of

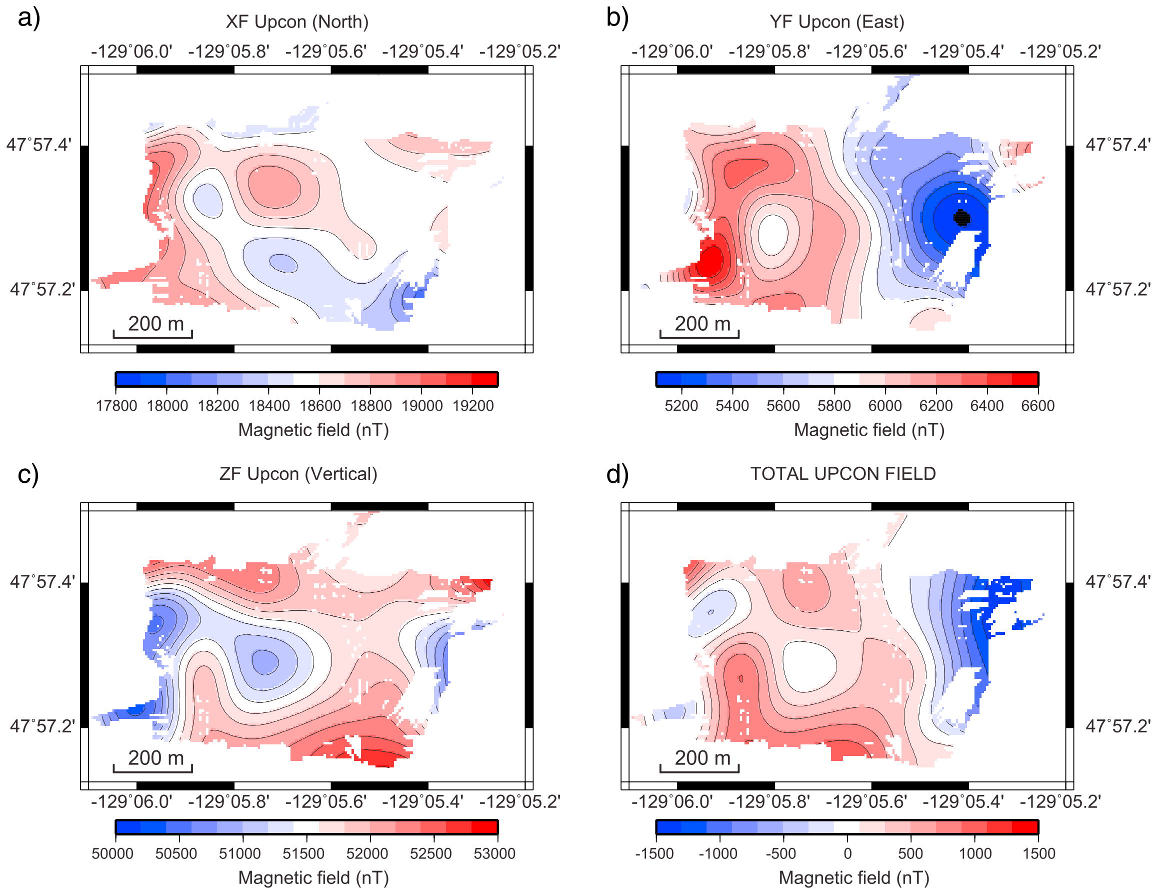

Figure 4. Panel of four maps showing the magnetic field component data continued upward to the 2070 m depth level (a) North, (b) East, (c) Vertical components and (d) the resultant Total magnetic field. Contour interval for the North and East components is 100 nT and 200 nT for the Vertical and Total field plots.

the vehicle. The orientation of ROV *Jason* (heading, pitch, and roll) is collected independent of the magnetic data using an Octans fiber optic gyro. The vehicle attitude information is then used in the calculation of the predicted magnetic field and in the correction of the measured magnetic field for the three magnetic field components: i.e., the North, East, and Vertical components. The vector sum of the three components gives the Total magnetic field.

The measured ROV magnetic field data were collected at 1 Hz and merged with the Octans attitude data based on the magnetic sensor time in addition to vehicle depth and altitude data collected by a Paroscientific and RDI Doppler sensor, respectively. The magnetic sensor data were corrected for the induced and permanent magnetic field effects of the ROV using the calibration approach established by *Isezaki* [1986], *Seama et al*. [1993], and *Korenaga* [1995], which is available from Tivey's website (http://deeptow.whoi.edu/download). In this approach, the observed magnetic field, $\boldsymbol{H}_{\text{obs}}$, is related to the local field plus the induced and permanent field effects using

$$\boldsymbol{H}_{\text{obs}} = RPY\boldsymbol{F} + ARPY\boldsymbol{F} + \boldsymbol{H}_p \tag{1}$$

Where $\boldsymbol{F}$ is the ambient geomagnetic field vector, A is the induced magnetization coefficient matrix, $\boldsymbol{H}_p$ is the permanent magnetic field vector of the vehicle, and R, P, and Y are, respectively, the rotation matrices of roll, pitch, and yaw (heading) of the vehicle. From *Korenaga* [1995] equation (1) can be rewritten as follows:

$$\beta\boldsymbol{H}_{\text{obs}} - \boldsymbol{H}'_{\text{p}} = RPY\boldsymbol{F} \tag{2}$$

where $\beta = (A+1)^{-1}$ and $\boldsymbol{H}'_p = \beta\,\boldsymbol{H}_p$. β and $\boldsymbol{H}'_p$ are estimated from the calibration spin data using a least squares inversion (or singular value decomposition). A and $\boldsymbol{H}'_{\text{p}}$ are assumed to be time invariant during the course of

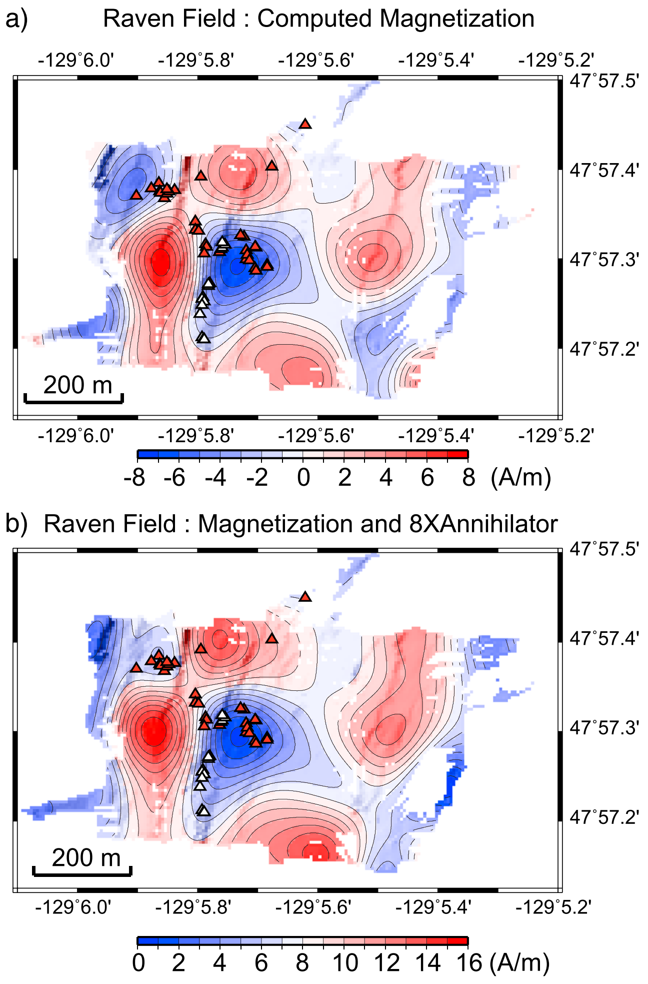

Figure 5. Contour maps of (a) the computed magnetization inversion (contour interval 1 A/m) and (b) computed magnetization with 8 times the annihilator added to the solution (contour interval 1 A/m). Maps have been given a background shading based on the slope of the underlying microbathymetry. Red and white triangles denote the location of the inactive and active vent sites, respectively [*Hearn et al.*, 2013].

the survey, and ***F*** can be approximated by the regional geomagnetic field vector estimated from the International Geomagnetic Reference Field (IGRF). A typical vehicle calibration spin performed in midwater above the dive site (~1200 m depth) gives a variation in total field of ~4600 nT, which is reduced to ~<150 nT after the calibration correction is applied. An example of calibration coefficients computed for ROV *Jason* dive 591 is shown below:

1. The induced field component matrix, β is

$$\begin{matrix} 1.01327 & 0.00950 & 0.03047 \\ 0.01313 & 0.98020 & -0.23218 \\ 0.00798 & 0.17869 & 0.92468 \end{matrix}$$

2. The permanent magnetic field vector offset, $\mathbf{H}'p$ in nT is

$$\begin{matrix} 1337.95 \\ 7222.50 \\ -5043.75 \end{matrix}$$

Following the calibration procedure, the three-component magnetic field data are merged with the navigational data. Navigation is based on doppler sonar positioning and ship-based Ultra-Short Baseline acoustic fixes. During ROV operations, the vehicle track varies its depth and height above the seafloor, and the magnetic field must be corrected for these variations in depth. Using a gridded approach, the three magnetic field components were interpolated onto grids with a 6 meter node spacing using a minimum curvature algorithm (GMT surface function: *Wessel and Smith* [1998]) (Figure 3 observed magnetic data components). The observed magnetic field shows the strongest magnetic intensity in the vertical component (Figure 3) consistent with the geomagnetic field at the latitude of this survey. A magnetic low is clearly present over the western wall and Raven vent field area in the observed vertical and total field components (Figures 3a and 3b).

Given the short time and relatively small area covered by the survey, a constant mean IGRF value for the region was removed from the observed magnetic field to obtain the anomaly field (IGRF 2011) [*Finlay et al.*, 2010]. To correct for the variable depth of ROV *Jason* above the seafloor we upward continue the observed magnetic field data to a level plane above the bathymetry. We used the Guspi Fourier transform upward continuation method [*Guspi*, 1987] to calculate magnetic field at a constant depth (−2070 m) above the terrain. Figure 4 shows the upward continued maps for the North, East, and Vertical components along with the Total magnetic field anomaly. The resultant fields (Figure 4) show smoothing compared to the observed fields (Figure 3) due to the filtering inherent in the upward continuation—we used a cosine band pass filter with a pass band between 750 m and 75 m spatial wavelengths. We used the *Parker and Huestis* [1974] Fourier inversion technique modified for three-dimensional grids (i.e., maps) by *Macdonald et al.* [1980] to compute the crustal magnetization (Figure 5a) using the upward continued total magnetic field. This method assumes a

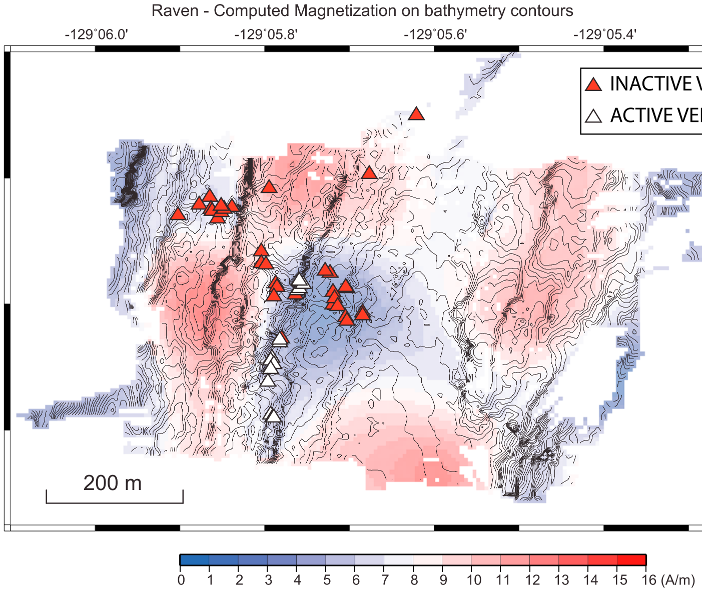

Figure 6. Final map image of crustal magnetization with 8 times the annihilator added to the solution to make the magnetization all positive. Overlaid contours are bathymetry (cont. int. 2 m). Red and white triangles denote the location of the inactive and active vent sites respectively [*Hearn et al.*, 2013]. Sun shading is from the multibeam bathymetry.

source layer of constant thickness with the upper surface defined by the bathymetry and magnetization invariant with depth. A fixed magnetic direction is used (Inclination = 68° and Declination = 17.6°) based on the IGRF and latitude and longitude of the study area. For this survey, we assumed a nominal 500 m thick source layer based on seismic estimates of the average thickness of Layer 2A in this area [*Van Ark et al.*, 2007], which is generally accepted as the primary source layer for crustal magnetization [*Harrison*, 1987]. Figure 5 shows the computed crustal magnetization.

One measure of the nonuniqueness of the inversion solution for crustal magnetization is the annihilator function—a magnetization distribution that when convolved with the bathymetry produces no lateral magnetic field variations [*Parker and Huestis*, 1974]. We calculate the annihilator function following the approach of *Macdonald et al.* [1980] by forward computing the field that results from using a 1 A/m source layer, inverting for crustal magnetization and taking the difference between the inversion and constant 1 A/m value. While an infinite amount of the resultant annihilator solution can be added to the magnetization inversion solution, only sufficient annihilator (8X) was applied to the magnetization inversion solution to make the inversion result positive, i.e., normal polarity, over the entire region (Figure 5b). The study area is well within the recent Brunhes normal polarity epoch, and so we expect no reversely magnetized crust for this region. The variation in annihilator is relatively minor so that the addition of annihilator to the magnetization only results in a shift in the mean magnetization value (see Figures 5a and 5b). The resultant magnetization solution plotted on top of bathymetry contours (Figure 6) shows that crustal magnetization varies between 0 and ~16 A/m, which is consistent with the magnetization of typical young oceanic crust [*Harrison*, 1987].

3.1. Vector Magnetic Analysis

Given that we collected vector magnetic data for this survey, we also investigated the ability and usefulness of calculating the magnetic gradient tensor from the three component data. The magnetic gradient tensor [*Nelson*, 1988; *Pederson and Rasmussen*, 1990] can be calculated from the spatial rate of change of the three field components (*Fx, Fy,* and *Fz*) along three orthogonal axes. For example, the tensor g_{xy} is the partial derivative of the *Fx* component in the *y* direction. See supporting information for details on the magnetic gradient tensor approach and a forward model example (Figures S1–S3) of a reduced magnetization zone within the Raven site. We applied these tensor techniques to the measured magnetic field data by calculating the magnetic gradient tensor components from the upward continued three component magnetic field data. Figure 7 shows the computed magnetic gradient tensor components, g_{xz}, g_{yz}, g_{xy}, and g_{zz} over the Raven

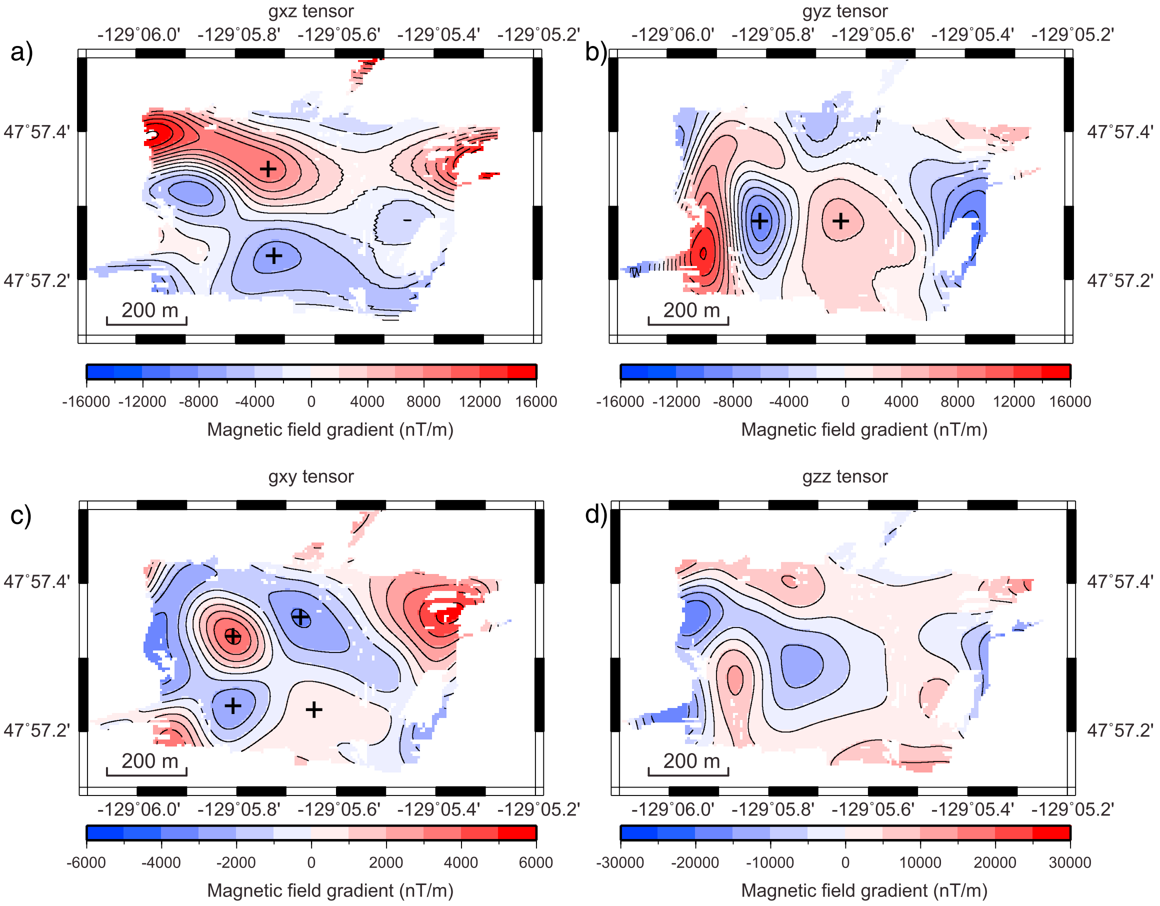

Figure 7. Panel of four maps showing the computed magnetic gradient tensor components for the Raven area (a) g_{xz} component, (b) g_{yz} component, (c) g_{xy} component, and d) the g_{zz} component. Black crosses mark magnetic highs and lows that are characteristic of a discrete source body at Raven (see supporting information for explanation). The contour interval for the g_{xz} and g_{yz} tensor components is 2000 nT/m, for the g_{xy} tensor component it is 1000 nT/m, and for the g_{zz} tensor it is 5000 nT/m.

area. As in the Raven forward model (Figure S3), the vertical gradient tensor component, g_{zz} shows the tightest concentration of contours around the demagnetized zone beneath the main Raven Field (Figure 7). Also, we see that the horizontal gradient tensor component g_{xy} shows the alternating peaks and lows of the corners/edges/extents of the source body quite effectively with the eastern edge being more diffuse similar to that imaged in the magnetization inversion result (compare Figures S3 and 7).

Magnetic field gradients can also be used for a simple depth estimation [*Miller and Singh*, 1994; *Salem et al.*, 2007] by using a tilt-depth method. The tilt-depth method uses a normalized ratio between the vertical, *z* and horizontal components, *h* of the total field, ***F***:

$$\theta = \arctan\left(\frac{\partial F}{\partial z}\bigg/\frac{\partial F}{\partial h}\right), \tag{3}$$

where

$$\frac{\partial F}{\partial h} = \sqrt{\left(\left(\frac{\partial F}{\partial x}\right)^2 + \left(\frac{\partial F}{\partial y}\right)^2\right)} \Rightarrow \sqrt{Gx^2 + Gy^2}. \tag{4}$$

The resultant tilt-angle map (Figure 8) of theta computed from the upward continued field shows contours from −90 to +90°. The edges of the source bodies are located at the 0° contour (assuming vertical boundaries) while the depth to the body is measured by the half width between the −45 to +45° contours. As can be seen in

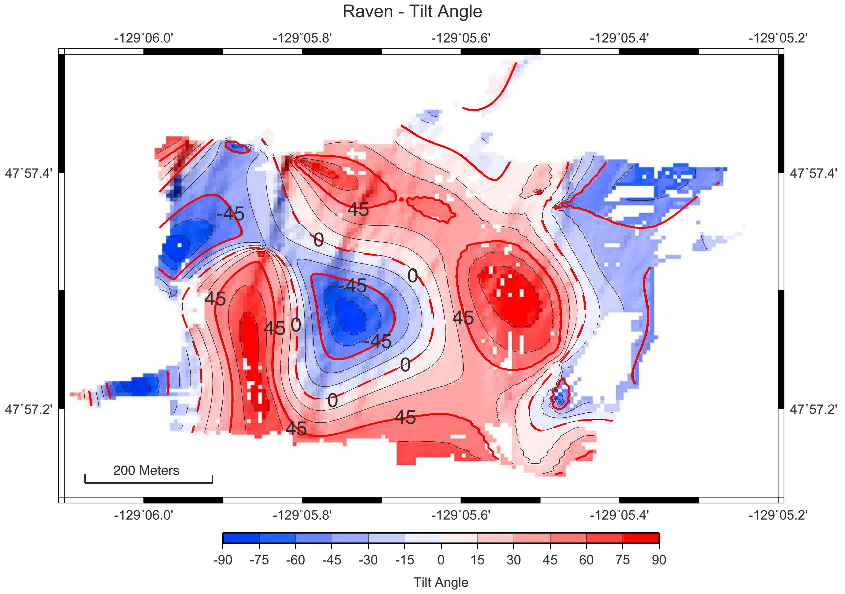

Figure 8. Tilt-angle and depth map for the Raven area computed from the ratio of the total field gradients as described in the text. Contour interval is 15°. The 0° contour (dashed) outlines the position of the source bodies, while the distance between the −45° and +45° contours (red lines) indicates the depth of the source body. Sun shading is from the multibeam bathymetry.

the tilt-depth map (Figure 8), the 0° contour clearly outlines the Raven vent field region as imaged in both the magnetization inversion (Figure 6) and the vertical gradient tensor, g_{zz} (Figure 7). Although, there is interference from nearby anomalies, the half width between the −45 and 45° contours varies between 25 and 63 m, which is, in effect, ROV *Jason* and magnetometer height above the seafloor. Thus, the demagnetized zone is consistent with a fluid upflow zone region that extends downward from the seafloor beneath the vent site. The basal depth of the zone is not resolved by this analysis.

Finally, we can estimate the volume of Layer 2A igneous crust associated with the inferred upflow zone beneath Raven vent area using the geometry provided by the first derivative of the vertical magnetic gradient tensor g_{zz} (Figure 7) or the zero angle of the tilt relationship (Figure 8). This zone can be approximated by 200 m diameter cylinder and assuming that the 500 m depth extent gives a volume of 15×10^6 m^3 of oceanic igneous crust that is hydrothermally altered due to upwelling hydrothermal fluid. This is likely an upper bound on the volume estimate because the magnetization inversion is averaged over the thickness of the assumed source layer, but the magnetization could also vary as a function of depth but that cannot be resolved in this approach —the inversion thus reflects the average properties.

4. Results and Discussion

We can compare the computed magnetization patterns to the seafloor geology that was photographically imaged during the same ROV *Jason* dives [*Hearn et al*., 2013]. From west to east across the rift valley, *Hearn et al.* [2013] define the upper west wall (UWW) (Figure 2b) of the rift valley as dominated by steep normal fault scarps tens of meters high associated with talus and broken pillow lava flows covered by thin pockets of sediment. At the base of the upper west wall is an uneven terrace that varies in width from south to north and is covered by more extensive sediments overlying broken pillow flow fragments. This terrace is divided into an upper terrace (UT) and lower terrace (LT) separated by a scissor fault (Figure 2b). The eastern edge of the lower terrace is bounded by the lower west wall (LWW), a steep fault scarp with a throw of 20 to 40 m with extensive talus and broken lava fragment at the base. This lower west wall is where the majority of the active hydrothermal venting is found (Figure 2b). A relatively flat axial valley floor (VF) extends horizontally 300 m to the eastern wall and consists of relatively complete sediment cover with minor faults, fissures, and flow fronts that interrupt the sediment cover to reveal pillow lava. The lower eastern wall (LEW) of the rift valley is marked by talus and broken lava on a series of successive fault ramps that step up to the east. *Hearn et al.* [2013] also identified

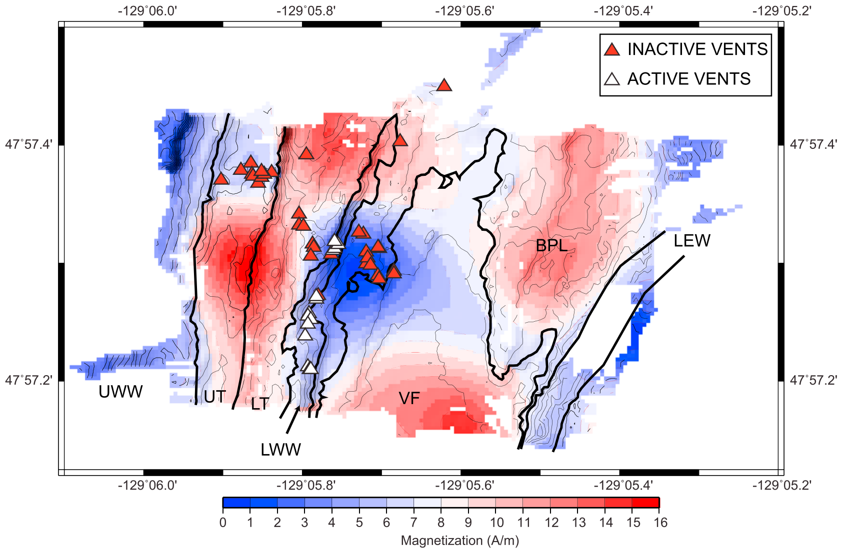

Figure 9. Summary map of Raven area showing the simplified geology and crustal magnetization map in color shading with overlaid bathymetry contours (5 m contour interval). Red and white triangles denote the location of the inactive and active vent sites, respectively [*Hearn et al.*, 2013]. Sun shading is from the multibeam bathymetry.

an area of broken pillow lava (BPL) with less sediment cover than the valley floor, forming a unit in the northeastern quarter of the rift valley (BPL zone, Figure 2b).

We can relate the tectonic and structural elements in terms of crustal magnetization (Figure 9). The upper western rift wall (UWW) has relatively weak magnetization compared with adjacent areas. The western upper terrace (UT) is marked by higher magnetization but with a discrete region of low magnetization that correlates with a cluster of inactive hydrothermal deposits at 47°57.375′N 129°5.9′W. The western lower terrace (LT) is marked by uniform higher magnetization, while the lower western wall (LWW) fault zone has markedly weaker magnetization. A zone of reduced magnetization associated with the active hydrothermal venting is present along the southern half of the wall (Figure 9) and extends eastward into a broader “bull’s-eye” magnetic low that is centered directly beneath the primary Raven hydrothermal area at 47°57.3′N 129°5.725′W (Figure 9). This low in magnetization has a sharply defined northern edge at 47°57.35′N 129°5.725′W but is more diffuse to the east and extends SE across the entire rift valley floor. In general, the rift valley floor is more strongly magnetized with the eastern side having the highest magnetization. A well-defined magnetic high in the NE quarter of the valley floor appears to correlate with a specific visually identified lava flow covered with broken pillow fragments (broken pillow flow, BPL, Figure 9). The eastern rift valley wall fault zone is relatively less magnetic, presumably reflecting the talus that dominates the area.

Overall, while the tectonically active and disrupted rift valley walls would be expected to be less magnetic than more coherently magnetized intact flows of the rift valley and terrace area, there is clearly an additional signal superimposed on this pattern by the hydrothermal activity. There is a clear correlation between the distribution of active hydrothermal venting and inactive vent deposits with zones of reduced magnetization (Figure 9). Furthermore, a distinctive SE to NW trend is discernable in both the crustal magnetization patterns and in the distribution of hydrothermal deposits, as noted by *Hearn et al.* [2013] and *Salmi et al.* [2014]. It has been noted [*Salmi et al.*, 2014] that this NW-SE alignment of the sulfide mineral deposits also corresponds with a shift in the location of the AMC from east to west between MEF and High Rise Field [*Van Ark et al.*, 2007] as well as a change in microearthquake focal mechanisms from normal to reverse faulting at the Raven Field just north of MEF [*Wilcock et al.*, 2009]. This trend suggests that a form of subsurface tectonic control on hydrothermal circulation has persisted for some time.

The general correlation between reduced crustal magnetization and hydrothermal activity in basaltic-hosted regions has been well documented [e.g., *Tivey et al.*, 1993; *Tivey and Johnson*, 2002; *Tivey and Dyment*, 2010; *Zhu et al.*, 2010; *Caratori-Tontini et al.*, 2012; *Honsho et al.*, 2013]. It is hypothesized that this correlation is primarily the result of alteration of the host rock with the highly corrosive hydrothermal fluid, altering the

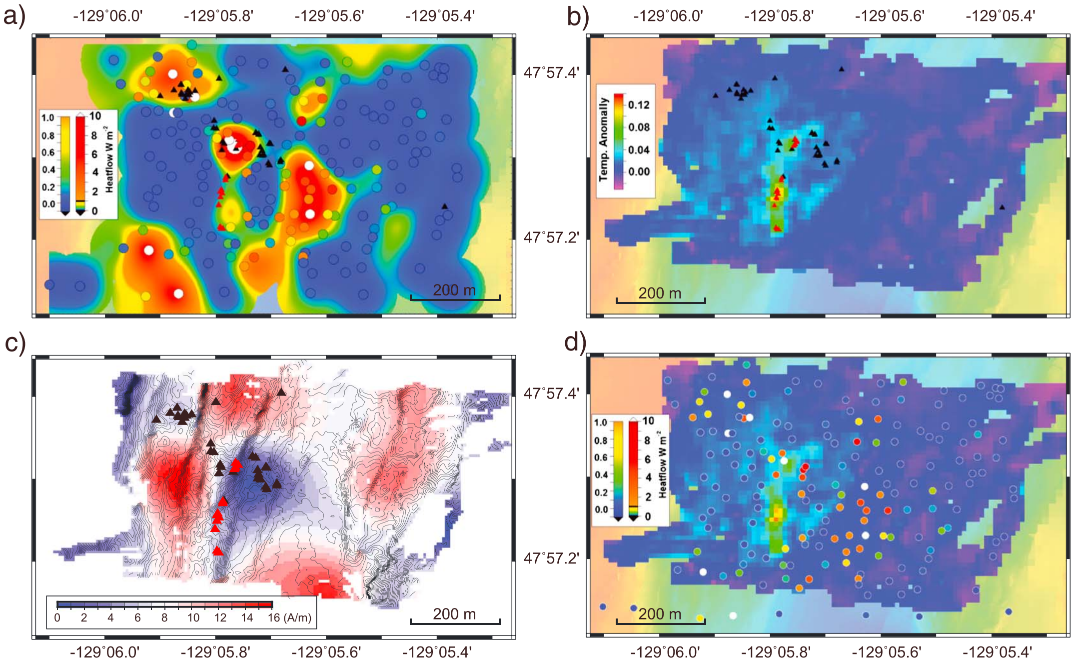

Figure 10. Compilation of conductive heat flux, bottom water temperature anomalies measured by ROV *Jason*, and the computed crustal magnetization: (a) conductive heat flux measurements and the interpolated heat flow map from *Salmi et al.* [2014]; (b) bottom water temperature anomalies from *Hearn et al.* [2013]; (c) crustal magnetization map from this study superimposed on bathymetric contours, and (d) bottom water temperature with the conductive heat flux stations superimposed. Figures 10a–10c denote the active vent sites by the red triangles and the inactive vent deposits by the black triangles.

magnetic mineral titanomagnetite that carries the magnetic signal in basaltic rock to less magnetic or nonmagnetic mineral phases [e.g., *Hochstein and Soengkono*, 1997; *Ade-Hall et al.*, 1971; *Watkins and Paster*, 1971]. Transient thermal demagnetization is also possible if the subsurface temperature beneath a vent site approaches the Curie temperature of the mineral carrying the magnetic signal (typically 150–200°C for titanomagnetite [*Dunlop and Ozdemir*, 1997], although the correlation of demagnetized zones with inactive vent sites suggests hydrothermal alteration at elevated temperatures as the primary mechanism for the crustal demagnetization.

4.1. Magnetics and Heat Flow

The Raven hydrothermal vent field is a relatively isolated and compact feature within the Endeavour rift valley and provides a unique opportunity to examine questions concerning the vertical and spatial geometry of the hydrothermal circulation system as well as the temporal relationships between present day activity and time-averaged effects. Insight into the present-day subsurface thermal structure of the study area is provided by the concurrent conductive heat flux study [*Salmi et al.*, 2014]. High conductive heat flow values are found associated with (a) the active Raven hydrothermal area, (b) along the lower west wall fault zone south of the main Raven complex, and (c) in the NW upper west wall region where a cluster of inactive hydrothermal deposits were observed (Figure 10a). Additionally, slightly higher heat flow is also found in the center of the rift valley where sediment thickness is sufficient to completely blanket and seal the underlying pillow lava (Figure 10a). Bottom water temperatures [*Hearn et al.*, 2013] map the location of the active vent sites in the Raven area and along the lower west wall (Figures 10b and 10d). In comparing the crustal magnetization patterns with the heat flow and bottom water temperature maps (Figure 10), we find a strong correlation between zones of reduced magnetization and the distribution of both active and inactive hydrothermal deposits as noted earlier (Figure 10c). Specifically, the central Raven magnetization low is centered over the main complex of inactive vent sites with the currently active vent site located toward the western side of the magnetization low on the rift valley wall. The reduced magnetization extends SW along the rift valley wall coincident with a zone of active vents and with a region of high heat flow and high bottom water temperatures (Figure 10). A zone of reduced magnetization also coincides with the inactive vent deposits in the NW (upper terrace) portion of the survey area, which is also an area of residual high heat flow (Figure 10). A more diffuse SE extension of the central Raven reduced magnetization zone extends across the axial valley and appears to correlate with the higher heat flow found in the central rift valley floor, presumably indicating a deeper subsurface fluid pathway that is continuing to affect both convective heat flux and crustal magnetization (Figure 10). From these comparisons, it is clear that the bottom water temperatures document the most recent active venting locations, while the heat flux patterns show areas of conductive heat flux associated with both active and inactive venting areas. The heat flux map (Figure 10a) has a greater spatial variability than the magnetization patterns (Figure 10) and thus we conclude that the heat flux measurements [*Salmi et al*., 2014] reflect the currently active thermal environment beneath the axial rift valley and near-ridge flanks, while the crustal magnetization is more representative of a time-averaged, permanent record of past hydrothermal alteration. The horizontal displacement of the highest temperature vent at the Raven vent site (by >100 m) between the 2001 [*Johnson et al*., 2002] and 2011 time periods [*Hearn et al*., 2013] demonstrates that seafloor and subseafloor permeability pathways can evolve relatively quickly. In contrast, the inactive vent deposits at the central Raven vent site have been dated to be at least 2000 years old [*Jamieson et al*., 2013] similar to some of the main vent fields on Endeavor (MEF, High Rise), indicating that activity at Raven field has been as persistent at this location, similar to nearby major vent fields. There are some isolated inactive vent deposits not associated with zones of reduced magnetization. The crustal magnetic response of these vent deposits may simply be below the resolution of the magnetic imaging or they possibly could have been short-lived systems that did not have enough time to produce significant reduced magnetization zones. Thus, in answer to one of our questions on the temporal relationship between present-day activity and the integrated effects over time, we conclude that reduced crustal magnetization zones are permanent features that reflect active alteration processes occurring over thousands of years while the heat flow data and the bottom water temperatures reflect the more transient effects that can migrate on a decadal scale.

In terms of the vertical and spatial geometry of the hydrothermal system at Raven, *Salmi et al*. [2014] interpret their heat flux measurements in terms of a dual-layer system composed of a thin uppermost high-permeability layer (seismic Layer 2A) vigorously convecting with small-dimension circulation cells and a deeper less permeable layer (seismic Layer 2B) that convects fluid slower and over longer distances that are bounded by the geometry of the rift valley, the bounding fault zones and the AMC geometry. *Salmi et al*. [2014] model the temperature regime within the crustal section both as a thermal gradient to the top of the AMC at 2300 m depth [*Van Ark et al*., 2007] and as a more realistic two-layer model with shallow vigorous hydrothermal circulation in the uppermost extrusive lava layer. In both cases, the temperature at the base of the extrusive lava seismic Layer 2A that comprises the magnetic source region would not reach the Curie or blocking temperatures for titanomagnetite (i.e., 300–580°C)—consistent with the conclusion that hydrothermal alteration, and not thermal demagnetization, is the major mechanism for the crustal demagnetization patterns. In addition to the upflow zones imaged beneath the main Raven Field, beneath an inactive hydrothermal zone on the upper west wall and beneath the active venting along the west rift valley wall areas, the main Raven Field is marked on its eastern side by a diffuse zone of reduced magnetization that extends eastward across the axial valley (Figures 6 and 10c). This extended diffuse zone of decreased magnetization strongly suggests that an across-axis pattern in fluid flow may be responsible for this distribution. The coincidence between this diffuse zone of reduced magnetization, the NW-SE trend in hydrothermal deposits, and the heat flux patterns (Figure 10) together suggest a deeper control on the circulation system likely constrained by the crustal architecture and axial magma chamber geometry at depth. As noted earlier, Raven Field is located just south of a shift in the AMC from east to west between MEF and High Rise Field [*Van Ark et al*., 2007] and a change in microearthquake focal mechanisms from normal to reverse faulting [*Wilcock et al*., 2009]. This across-axis geometry in fluid circulation is consistent with *Johnson et al*. [2010] who also concluded that the across-axis variation AMC depth helps drive the across-axis circulation patterns in an area just south of Raven Field. In this survey, we also find that along-axis crustal structure may also constrain the geometry of the across-axis circulation patterns.

5. Conclusions

A survey of near-bottom magnetic anomalies of the Raven hydrothermal field within the axial valley of Endeavour Segment of the Juan de Fuca Ridge with dense track line coverage was combined with coregistered data from heat flow measurements, bottom water temperature anomalies, and photographic estimates of seafloor permeability to construct a model of subsurface pathways of subsurface hydrothermal fluid flow. The dense grid of magnetic data acquisition allows for identification of those regions within the seismic Layer 2A upper igneous crust that have been exposed to hydrothermal alteration at elevated temperatures. Discrete areas of reduced magnetization of the axial valley floor and flanking valley walls are associated with both active and inactive hydrothermal vent deposits, areas of high conductive heat flow [*Salmi et al.*, 2014] and near-bottom water temperature anomalies [*Hearn et al.*, 2013]. Downward continuation of the geothermal gradient from the conductive heat flow data [*Salmi et al.*, 2014] suggest that the subsurface temperatures in the zones of reduced magnetization are not sufficiently elevated to thermally demagnetize the crust on the scale observed and that chemical alteration of the magnetic mineralogy is the primary mechanism. Regions of the axial valley with the high magnetization normally associated with recent crustal formation are either regions of seawater recharge for the crustal fluid cells or were sealed from any fluid transmission by near 100% sediment cover.

The assumption of a convecting layer hosted within the volcanic extrusives of the upper crust is primarily seismically defined Layer 2A, as the magnetic anomaly inversions do not provide unique constraints on the lower bound. The acquisition of vector magnetic data does allow for tensor calculations to be made that effectively provide tighter constraints on source regions of alteration within this layer. These calculations indicate that the hydrothermally altered zone beneath the Raven Field is approximately 15×10^6 m^3 in volume, which is an upper bound.

Finally, a more diffuse zone of reduced crustal magnetization extending from NW to SE across rift valley floor from the Raven Field to the eastern valley wall (Figures 6 and 10c) is consistent with an additional deeper circulation cell possibly below Layer 2A. This isolated limb of a deeper cross-axis cell may be controlled by sub-Layer 2A crustal architecture on the fluid circulation patterns within the larger Endeavour axial valley. The across-axis flow modeled by *Johnson et al.* [2010] for just north of MEF and by *Salmi et al.* [2014] for the Raven Field is supported by the presence of the cross-axis reduced magnetization zone (Figure 10) and may represent narrow channels of fluid circulation. Circulation in these cross-valley channels would be driven by the thermal gradient from the tilted subsurface magma chamber that underlies the valley and the flow constrained by isolated zones of high crustal permeability. From the distribution of magnetization (Figure 10), these deeper cross-axis channels do not appear to be present in the valley north of the Raven Field.

Acknowledgments
The paper benefited from reviews by Mark Dekkers, Claire Bouligand, and Supri Soengkono. We would like to thank Captain Allan Lunt, Expedition Leader Tito Collasius, and the crew of ROV *Jason* II and R/V *Atlantis* for their efforts in making the 2011 Expedition: AT18-09 cruise a success. M.T. and H.P.J. wish to thank Casey Hearn and Kira Homola, and the rest of the University of Washington students of the Scientific Party as well as graduate student Will Fortin of the University of Wyoming for their participation and help during the cruise. We thank Tor Bjorklund, who was instrumental in designing and building the thermal blankets used during the program. This work was funded by the National Science Foundation under grant OCE-1037840 to Maurice Tivey and grant OCE-1037870 to H. Paul Johnson. The raw *Jason* ROV digital data used in this study are available upon request from the National Deep Submergence Facility at Woods Hole Oceanographic Institution (NDSFdatmgr@whoi.edu). *Jason* video imagery is available through the Virtual van website (http://4dgeo.whoi.edu/Jason/). Derived products and maps used in this work are available upon request from the lead author at mtivey@whoi.edu.

References

Ade-Hall, J. M., H. C. Palmer, and T. P. Hubbard (1971), The magnetic and opaque petrological response of basalt to regional hydrothermal alteration, *Geophys. J. R. Astron. Soc.*, *24*, 137–174.

Alt, J. C. (1995), Subseafloor processes in mid-ocean ridge hydrothermal systems, in *Seafloor Hydrothermal Systems: Physical, Chemical, Biological, and Geological Interactions*, *Geophys. Monogr. Ser.*, vol. 91, edited by S. E. Humphris et al., pp. 85–114, AGU, Washington, D. C.

Browne, P. R. L. (1978), Hydrothermal alteration in active geothermal fields, *Annu. Rev. Earth Planet. Sci.*, *6*, 229–250.

Caratori-Tontini, F., B. Davy, C. E. J. de Ronde, R. W. Embley, M. Leybourne, and M. A. Tivey (2012), Crustal magnetization of Brothers volcano, New Zealand, measured by autonomous underwater vehicles: Geophysical expression of a submarine hydrothermal system, *Econ. Geol.*, *107*, 1571–1581, doi:10.2113/econgeo.107.8.1571.

Carbotte, S. M., R. S. Detrick, J. P. Canales, A. J. Harding, G. M. Kent, J. Babcock, M. R. Nedimović, J. B. Diebold, and E. van Ark (2006), Magmatic-tectonic episodicity at oceanic spreading centers revisited, *Geology*, *34*, 209–212, doi:10.1130/G21969.1.

Carbotte, S. M., J. P. Canales, M. R. Nedimović, H. Carton, and J. C. Mutter (2012), Recent seismic studies at the East Pacific Rise 8°20′–10°10′N and Endeavour Segment: Insights into mid-ocean ridge hydrothermal and magmatic processes, *Oceanography*, *25*(1), 100–112, doi:10.5670/oceanog.2012.08.

Chen, Y. J., and J. P. Morgan (1996), The effects of spreading rate, the magma budget, and the geometry of magma emplacement on the axial heat flux at mid-ocean ridges, *J. Geophys. Res.*, *101*, 11,475–11,482, doi:10.1029/96JB00330.

Childress, J. J., and C. R. Fisher (1995), The biology of hydrothermal vent animals: Physiology, biochemistry, and autotrophic symbioses, *Oceanogr. Mar. Biol. Annu. Rev.*, *30*, 337–441.

Clague, D. A., D. W. Caress, H. Thomas, D. Thompson, M. Calarco, J. Holden, and D. Butterfield (2008), Abundance and distribution of hydrothermal chimneys and mounds on the Endeavour Ridge determined by 1-m resolution AUV multibeam mapping surveys. *Eos Trans. AGU*, *89*(53), Abstract V41B-2079.

Coumou, D., T. Driesner, and C. A. Heinrich (2008), The structure and dynamics of mid-ocean ridge hydrothermal systems, *Science*, *321*, 1825–1828, doi:10.1126/science.1159582.

Delaney, J. R., V. Robigou, R. E. McDuff, and M. K. Tivey (1992), Geology of a vigorous hydrothermal system on the Endeavour Segment, Juan de Fuca Ridge, *J. Geophys. Res.*, *97*(B13), 19,663–19,682, doi:10.1029/92JB00174.

Delaney, J. R., D. S. Kelley, M. D. Lilley, D. A. Butterfield, R. E. McDuff, J. A. Baross, J. W. Deming, H. P. Johnson, and V. Robigou (1997), The Endeavour hydrothermal system: Part I. Cellular circulation above an active cracking front yields large sulfide structures, “fresh” vent water, and hyperthermophile archaea, *RIDGE Events*, *8*, 11–19.

Dunlop, D. J., and O. Ozdemir (1997), *Rock Magnetism, Fundamentals and Frontiers*, 573 pp., Cambridge Univ. Press, Cambridge, U. K.

Finlay, C. C., et al. (2010), International Geomagnetic Reference Field: The eleventh generation, International Association of Geomagnetism and Aeronomy, Working Group V-MOD, *Geophys. J. Int.*, *183*, 1216–1230.

Fontaine, F. J., and W. S. D. Wilcock (2007), Two-dimensional models of hydrothermal convection at high Rayleigh and Nusselt numbers: Implications for mid-ocean ridges, *Geochem. Geophys. Geosyst.*, *8*, Q07010, doi:10.1029/2007GC001601.

Glickson, D., D. S. Kelley, J. R. Delaney (2007), Geology and hydrothermal evolution of the Mothra hydrothermal field, Endeavour segment, Juan de Fuca Ridge, *Geochem. Geophys. Geosyst.*, *8*, Q06010, doi:10.1029/2007GC001588.

Guspi, F. (1987), Frequency-domain reduction of potential field measurements to a horizontal plane, *Geoexploration*, *24*, 87–98.

Hall, J. M. (1992), Interaction of submarine volcanic and high-temperature hydrothermal activity proposed for the formation of the Agrokipia volcanic massive sulfide deposits of Cyprus, *Can. J. Earth Sci.*, *29*, 1928–1936.

Hannington, M. D., C. E. J. De Ronde, and S. Petersen (2005), Sea-floor tectonics and submarine hydrothermal systems, *Econ. Geol.*, *100*, 111–141.

Harrison, C. G. A. (1987), Marine magnetic anomalies—The origin of the stripes, *Annu. Rev. Earth Planet. Sci.*, *15*, 505–543.

Hearn, C. K., K. L. Homola, and H. P. Johnson (2013), Surficial permeability of the axial valley seafloor: Endeavour Segment, Juan de Fuca Ridge, *Geochem. Geophys. Geosyst.*, *14*, 3409–3424, doi:10.1002/ggge.20209.

Hochstein, M. P., and S. Soengkono (1997), Magnetic anomalies associated with high temperature reservoirs in the Taupo volcanic zone (New Zealand), *Geothermics*, *26*(1), 1–24.

Honsho, C. E., T. Ura, and K. Kim (2013), Deep-sea magnetic vector anomalies over the Hakurei hydrothermal field and the Bayonnaise knoll caldera, Izu-Ogasawara arc, Japan, *J. Geophys. Res. Solid Earth*, *118*, 5147–5164, doi:10.1002/jgrb.50382.

Irving, E. (1970), The mid-Atlantic ridge at 45 N, XIV. Oxidation and magnetic properties of basalt; review and discussion, *Can. J. Earth Sci.*, *7*, 1528–1538.

Isezaki, N. (1986), A new shipboard three component magnetometer, *Geophysics*, *51*, 1992–1998.

Jamieson, J. W., M. D. Hannington, D. A. Clague, D. S. Kelley, J. R. Delaney, J. F. Holden, M. K. Tivey, and L. E. Kimpe (2013), Sulfide geochronology along the Endeavour Segment of the Juan de Fuca Ridge, *Geochem. Geophys. Geosyst.*, *14*, 2084–2099, doi:10.1002/ggge.20133.

Johnson, H. P., and T. Atwater (1977), Magnetic study of basalts from the Mid-Atlantic ridge, lat. 37°N, *Geol. Soc. Am. Bull.*, *88*, 637–647.

Johnson, H. P., and M. Hutnak (1997), Conductive heat loss in recent eruptions at mid-ocean ridges, *Geophys. Res. Lett.*, *24*, 3089–3092, doi:10.1029/97GL02998.

Johnson, H. P., and R. T. Merrill (1972), Magnetic and mineralogical changes associated with the low-temperature oxidation of magnetite, *J. Geophys. Res.*, *77*, 334–341, doi:10.1029/JB077i002p00334.

Johnson, H. P., and R. T. Merrill (1973), Low-temperature oxidation of a titanomagnetite and implications for paleomagnetism, *J. Geophys. Res.*, *78*, 4938–4949, doi:10.1029/JB078i023p04938.

Johnson, H. P., J. L. Karsten, F. J. Vine, G. C. Smith, and G. Schonharting (1982), A low-level magnetic survey over a massive sulfide ore body in the Troodos ophiolite complex, Cyprus, *Mar. Technol. Soc. J.*, *16*, 76–79.

Johnson, H. P., S. L. Hautala, M. A. Tivey, C. D. Jones, J. Voight, M. Pruis, and I. Garcia-Berdeal (2002), Survey studies hydrothermal circulation on the northern Juan de Fuca Ridge, *Eos Trans. AGU*, *83*(8), 73–79, doi:10.1029/2002EO000043.

Johnson, H. P., M. A. Tivey, T. A. Bjorkland, and M. S. Salmi (2010), Hydrothermal circulation within the Endeavour Segment; Juan de Fuca Ridge, *Geochem. Geophys. Geosyst.*, *11*, Q05002, doi:10.1029/2009GC002957.

Kelley, D. S., et al. (2012), Endeavour Segment of the Juan de Fuca Ridge: One of the most remarkable places on Earth, *Oceanography*, *25*(1), 44–61, doi:10.5670/oceanog.2012.03.

Korenaga, J. (1995), Comprehensive analysis of marine magnetic vector anomalies, *J. Geophys. Res.*, *100*, 365–378, doi:10.1029/94JB02596.

Lowell, R. P., A. Farough, L. N. Germanovich, L. B. Hebert, and R. Horne (2012), A vent-field-scale model of the East Pacific Rise 9°50′N magma-hydrothermal system, *Oceanography*, *25*(1), 158–167, doi:10.5670/oceanog.2012.13.

Lowell, R. P., A. Farough, J. Hoover, and K. Cummings (2013), Characteristics of magma-driven hydrothermal systems at oceanic spreading centers, *Geochem. Geophys. Geosyst.*, *14*, 1756–1770, doi:10.1002/ggg.20109.

Macdonald, K. C., S. P. Miller, S. P. Huestis, and F. N. Spiess (1980), Three-dimensional modeling of a magnetic reversal boundary from inversion of deep-tow measurements, *J. Geophys. Res.*, *85*, 3670–3680, doi:10.1029/JB085iB07p03670.

Miller, H. G., and V. Singh (1994), Potential field tilt—A new concept for location of potential field sources, *J. Appl. Geophys.*, *32*, 213–217.

Mottl, M. J. (2003), Partitioning of energy and mass fluxes between mid-ocean ridge axes and flanks at high and low temperature, in *Energy and Mass Transfer in Marine Hydrothermal Systems*, edited by P. E. Halbach, V. Tunnicliffe, and J. R. Hein, pp. 271–286, Dahlem Univ. Press, Berlin.

Nelson, J. B. (1988), Calculation of the magnetic gradient tensor from total field gradient measurements and its application to geophysical interpretation, *Geophysics*, *53*, 957–966.

Parker, R. L., and S. P. Huestis (1974), The inversion of magnetic anomalies in the presence of topography, *J. Geophys. Res.*, *79*, 1587–1594, doi:10.1029/JB079i011p01587.

Pederson, L. B., and T. M. Rasmussen (1990), The gradient tensor of potential field anomalies: Some implications on data collection and data processing of maps, *Geophysics*, *55*(12), 1558–1566.

Phipps Morgan, J., and Y. J. Chen (1993), The genesis of oceanic crust: Magma injection, hydrothermal circulation and crustal flow, *J. Geophys. Res.*, *98*, 6283–6297, doi:10.1029/92JB02650.

Rabinowicz, M., J.-C. Sempéré, and P. Genthon (1999), Thermal convection in a vertical permeable slot: Implications for hydrothermal circulation along mid-ocean ridges, *J. Geophys. Res.*, *104*, 29,275–29,292, doi:10.1029/1999JB900259.

Richards, H. G., J. R. Cann, and J. Jensensius (1989), Mineralogical zonation and metasomatism of the alteration pipes of Cyprus sulfide deposits, *Econ. Geol.*, *84*, 91–115.

Rona, P. A. (1978), Magnetic signatures of hydrothermal alteration and volcanogenic mineral deposits in oceanic crust, *J. Volcanol. Geotherm. Res.*, *3*, 219–225.

Salem, A., S. Williams, J. D. Fairhead, D. Ravat, and R. Smith (2007), Tilt-depth method: A simple depth estimation method using first-order magnetic derivatives, *Leading Edge*, *26*(12), 1502–1505.

Salmi, M. S., H. Paul Johnson, M. A. Tivey, and M. Hutnak (2014), Quantitative estimate of heat flow from a mid-ocean ridge axial valley, Raven field, Juan de Fuca Ridge: Observations and inferences, *J. Geophys. Res. Solid Earth*, *119*, doi:10.1002/2014JB011086.

Seama, N., Y. Nogi, and N. Isezaki (1993), A new method for precise determination of the position and strike of magnetic boundaries using vector data of the geomagnetic anomaly field, *Geophys. J. Int.*, *113*, 155–164.

Spinelli, G. A., and A. T. Fisher (2004), Hydrothermal circulation within topographically rough basaltic basement on the Juan de Fuca Ridge flank, *Geochem. Geophys. Geosyst.*, *5*, Q02001, doi:10.1029/2003GC000616.

Stein, C., and S. Stein (1994), Constraints on hydrothermal heat-flux through the oceanic lithosphere from global heatflow, *J. Geophys. Res.*, *99*(B2), 3081–3095, doi:10.1029/93JB02222.

Studt, F. E. (1959), Magnetic survey of the Wairakei hydrothermal field, *N. Z. J. Geol. Geophys.*, *2*, 746–754.

Tivey, M. A., and J. Dyment (2010), The magnetic signature of hydrothermal systems in slow-spreading environments, in *Diversity of Hydrothermal Systems on Slow Spreading Ridges*, *Geopys. Monogr. Ser.*, vol. 188, edited by P. Rona et al., pp. 43–66, AGU, Washington, D. C., doi:10.1029/2008GM000773.

Tivey, M. A., and H. P. Johnson (2002), Crustal magnetization reveals subsurface structure of Juan de Fuca Ridge hydrothermal vent fields, *Geology*, *30*, 979–982.

Tivey, M., P. A. Rona, and H. Schouten (1993), Reduced crustal magnetization beneath the active sulfide mound, TAG hydrothermal field, Mid-Atlantic Ridge, at 26°N, *Earth Planet. Sci. Lett.*, *115*, 101–115.

Tivey, M. A., P. A. Rona, and M. C. Kleinrock (1996), Reduced crustal magnetization beneath relict hydrothermal mounds of the TAG hydrothermal field, Mid-Atlantic Ridge, 26°N, *Geophys. Res. Lett.*, *23*, 3511–3514, doi:10.1029/96GL02082.

Tivey, M. A., H. Schouten, and M. C. Kleinrock (2003), A near-bottom magnetic survey of the Mid-Atlantic Ridge axis at 26°N: Implications for the tectonic evolution of the TAG segment, *J. Geophys. Res.*, *108*(B5), 2277, doi:10.1029/2002JB001967.

Van Ark, E. M., R. S. Detrick, J. P. Canales, S. M. Carbotte, A. J. Harding, G. M. Kent, M. R. Nedimovic, W. S. D. Wilcock, J. B. Diebold, and J. M. Babcock (2007), Seismic structure of the Endeavour Segment, Juan de Fuca Ridge: Correlations with seismicity and hydrothermal activity, *J. Geophys. Res.*, *112*, B02401, doi:10.1029/2005JB004210.

Watkins, N. D., and T. P. Paster (1971), The magnetic properties of igneous rocks from the ocean floor, *Philos. Trans. R. Soc. London, Ser. A*, *268*, 507–550.

Wessel, P., and W. H. F. Smith (1998), New, improved version of the Generic Mapping Tools released, *Eos Trans. AGU*, *79*(47), 579, doi:10.1029/98EO00426.

Wilcock, W. S. D. (1998), Cellular convection models of mid-ocean ridge hydrothermal circulation and the temperatures of black smoker fluid, *J. Geophys. Res.*, *103*, 2585–2596, doi:10.1029/97JB03252.

Wilcock, W. S. D., and J. R. Delaney (1996), Mid-ocean ridge sulfide deposits: Evidence for heat extraction from magma chambers or cracking fronts?, *Earth Planet. Sci. Lett.*, *145*, 49–64.

Wilcock, W. S. D., E. E. E. Hooft, D. R. Toomey, P. R. McGill, A. H. Barclay, D. S. Stakes, and T. M. Ramirez (2009), The role of magma injection in localizing blacksmoker activity, *Nat. Geosci.*, *2*, 509–513, doi:10.1038/NGEO550.

Wooldridge, A. L., S. E. Haggerty, P. A. Rona, and C. G. A. Harrison (1990), Magnetic properties and opaque mineralogy of rocks from selected seafloor hydrothermal sites at oceanic ridges, *J. Geophys. Res.*, *95*(B8), 12,351–12,374, doi:10.1029/JB095iB08p12351.

Zhu, J., J. Lin, Y. J. Chen, C. Tao, C. R. German, D. R. Yoerger, and M. A. Tivey (2010), A reduced crustal magnetization zone near the first observed active hydrothermal vent field on the southwest Indian Ridge, *Geophys. Res. Lett.*, *37*, L18303, doi:10.1029/2010GL043542.